Journal of Materials Processing Technology 229 (2016) 128–138

Contents lists available at ScienceDirect

Journal of Materials Processing Technology

journal homepage: www.elsevier.com/locate/jmatprotec

Dimensional accuracy of Electron Beam Melting (EBM) additive manufacture with regard to weight optimized truss structures

C.J. Smith[a,*], F. Derguti[b], E. Hernandez Nava[b], M. Thomas[b], S. Tammas-Williams[c], S. Gulizia[d], D. Fraser[d], I. Todd[b]

[a] Department of Civil & Structural Engineering, University of Sheffield, Mappin Street, Sheffield S1 3JD, UK
[b] Department of Materials Science & Engineering, University of Sheffield, Mappin Street, Sheffield S1 3JD, UK
[c] Materials Science Building, School of Materials, The University of Manchester, Manchester M13 9PL, UK
[d] CSIRO Manufacturing Flagship, Gate 3 Normanby Rd, Clayton, 3169 VIC, Australia

ARTICLE INFO

Article history:
Received 18 November 2014
Received in revised form 26 August 2015
Accepted 27 August 2015
Available online 1 September 2015

Keywords:
Laser scanning
X-ray tomography
Titanium
Arcam
Topology optimization
Truss structures

ABSTRACT

The Electron Beam (EBM) additive manufacturing process is well suited to fabricating complex structural designs in Ti–6Al–4V because of the design freedoms it offers combined with strong and consistent material properties. However it has been observed that complications may arise when manufacturing truss-like structures (such as those produced via structural topology optimization) in the form of undersized features on the finished part. The issue appears to affect truss members that are not aligned with the vertical build direction, with an apparent lack of material on the negative surfaces. This effect appears to worsen with a greater angle between the truss member and the build direction, even with the use of support structures. This investigation has characterized and measured the dimensional errors that result from this issue through 3D scanning techniques. Process modifications have then been made which result in significant improvements in dimensional accuracy. This investigation highlights the importance of heat management at features with negative surfaces to yield parts that are dimensionally accurate without introducing excessive internal melt defects in the form of voids and porosity.

1. Introduction

Additive manufacturing (AM) offers a significant degree of design freedom when compared with conventional manufacturing routes. One of the many exciting applications of AM is the realisation of minimal mass structures designed using structural topology optimisation, a computational design method. Established Finite Element based topology optimization methods are detailed in recent reviews by Rozvany (2009) and Sigmund and Maute (2013), with the former detailing some of the commercialization of these methods. Through structural topology optimization significant weight reductions can be achieved over conventionally designed parts by ensuring the material that constitutes the structure is used more efficiently; hence topology optimised structures will ideally have a homogeneous stress distribution or can be thought of as fully stressed at their maximum design load (for a single load case). Generally designs of this nature are very complex which may result in structural performance that is very sensitive to the dimensional accuracy of the finished part. With little in the way of redundant material, any undersized features will be subject to higher stress with the consequence that premature failure of the entire structure may result.

When manufacturing test specimens designed to evaluate the accuracy of Computer Numerically Controlled (CNC) machining processes, Cooke and Soons (2010) found that both EBM and laser processes incurred dimensional errors at least an order of magnitude higher than their machined counterparts. Specifically Cansizoglu et al. (2008) and more recently Smith et al. (2015) observed that the EBM process tends to fabricate truss structures with undersized members, particularly those at an angle to the build direction. The observed error seems to mostly occur in regions with no prior melted material beneath them, generally referred to as *negative surfaces*. Two examples of features with negative surfaces are illustrated in Figs. 2a and b, which show a ledge overhang and an angled surface respectively. These features are generally problematic for metallic powder bed AM processes as the lower thermal conductivity of the powder beneath them results in a great deal of heat accumulation leading to part distortion. Porous support structures which usually comprise thin walls (~0.5 mm thick) or rods (~0.8 mm in diameter) are generally placed at negative

* Corresponding author. Tel.: +44 114 2226035.
E-mail address: chrisjsmith@sheffield.ac.uk (C.J. Smith).

http://dx.doi.org/10.1016/j.jmatprotec.2015.08.028

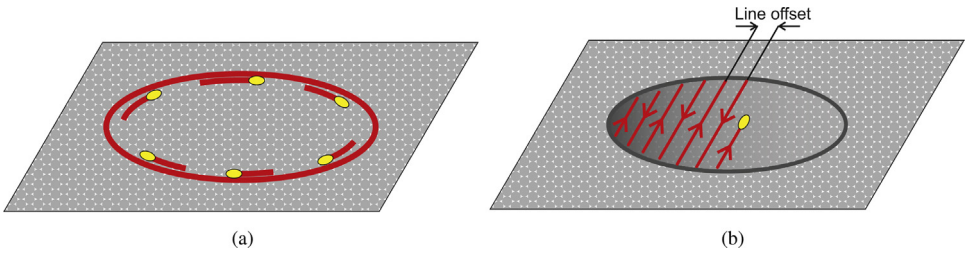

Fig. 1. (a) Contour and (b) hatch stage of the melt.

surfaces to provide improved heat conduction away from the melt region and are relatively easy to remove post-build. However even when using such structures this particular issue still seems to persist.

The in-service performance implications of undersized members in fully stressed truss structures are potentially very serious. A decrease in cross-sectional area will result in a reduced axial load capacity of the member. Additionally, with material lacking on only one side of the member the second moment of area will be reduced and an effective curvature introduced in an otherwise linear member. Both of these will reduce the resistance to buckling. Just one undersized member can compromise the performance of an entire structure. Thus developing design methods that reduce the sensitivity of topology optimised structures to manufacturing defects has become an active area of research. Schevenels et al. (2011), have for example, made use of probabilistic methods to produce more robust topology optimised designs that are less sensitive to the random dimensional errors that occur during manufacturing. The dimensional errors observed for components manufactured by the EBM process do not appear entirely random however and it is therefore likely that these could instead be significantly reduced through process modifications rather than through statistical approaches.

When modifying the process parameters of the EBM process to maintain accuracy it is, however, important to assess the quality of the resulting microstructure, particularly with regard to the presence of internal voids and porosity. In common with laser powder bed AM, the EBM process is known to produce parts with a certain degree of porosity, but these pores are usually small (<100 μm) and their origins are known to be related to trapped gas during the manufacture of the powder or the result of lack of fusion (Tammas-Williams et al., 2015). Their presence is still significant enough to affect fatigue life (as shown experimentally by Edwards et al., 2013) and can be removed by Hot Isostatic Pressing (HIPing). Larger voids can present themselves if insufficient energy is directed into the melt pool, as modelled and shown experimentally by Bauereiß et al. (2014).

To understand these issues affecting complex truss structures, this investigation seeks to probe the capability limits of the EBM process through the manufacture of simple truss specimens. As follows:

1 Quantify the dimensional accuracy for arbitrary truss structures fabricated using the default process parameters as provided by the manufacturer (Arcam) to act as a benchmark. The dimensional accuracy is assessed for members of several diameters over a range of angles relative to the build direction.
2 The dimensions to be quantified are those directly related to the structural performance of truss structures i.e. cross-sectional area, second moment of area and curvature of each truss member.
3 Attempt to improve dimensional accuracy for single truss members at the largest angle to the build direction explored in the benchmark build by systematic modification of the beam process parameters.
4 Apply the process parameters yielding the best results to the benchmark experiment in step 1 and assess changes in dimensional accuracy that result.
5 Assess the quality of the microstructure (presence of voids and porosity) produced using the modified process parameters.

2. EBM process and the thickness function

After powder deposition, the EBM process will preheat (and sinter) the present layer to a specified target temperature (720 °C in this case) by scanning the beam across the entire layer at high velocity. The amount of energy required to maintain this temperature is determined by solving a one dimensional thermal model that balances the energy input (based on the area to be melted) with the energy lost by conductance through the powder bed. Once preheating has completed the part cross-section(s) are melted in two stages referred to as *contouring* and *hatching*. *Contouring*, which is used to improve the surface finish of the part, melts the perimeter of the part cross-section using a constant beam power and velocity (as illustrated in Fig. 1a). Typically this is done using two passes concentrically offset from one another (referred to as the inner and outer *contouring*). The near instantaneous deflection of the electron beam is used to maintain multiple melt pools simultaneously to reduce the time spent on this stage.

The majority of the melting is performed using *hatching*, which can follow or precede *contouring*. *Hatching* employs a back and forth raster pattern as shown in Fig. 1b which, unlike *contouring*, does not use a constant beam power and velocity throughout the build. These two parameters are instead varied to attain consistent melt properties in the face of changing thermal conditions during melting. In total four analytical expressions are evaluated to determine the beam power and velocity to achieve this. The first, referred to as the current compensation algorithm will set the beam current (power) based on the length of the hatch line. With the back and forth raster pattern, a longer hatch line will have a different thermal history to a shorter one, with the former taking longer to complete and thus requiring more energy input to account for the resulting heat dissipation. A follow-up function known as the speed function will then set the beam velocity based on this beam current to ensure the melt pool is always a constant size regardless of hatch line length.

The remaining two functions reduce the beam energy at input at locations where there will be significant heat accumulation. The first, known as the turning point function, will reduce the beam energy input near the start of each hatch line. This is because the start point of each hatch line is adjacent to the end point of the previous hatch line and thus with no time for the heat to dissipate the beam energy input must be reduced to prevent excessive heat accumulation. Finally the thickness function, which is the area of interest for this study, will reduce the beam energy input when melting in proximity to a negative surface. This is to account for the lower thermal conductivity of the sintered powder beneath negative surfaces. As only this function will be modified in this study

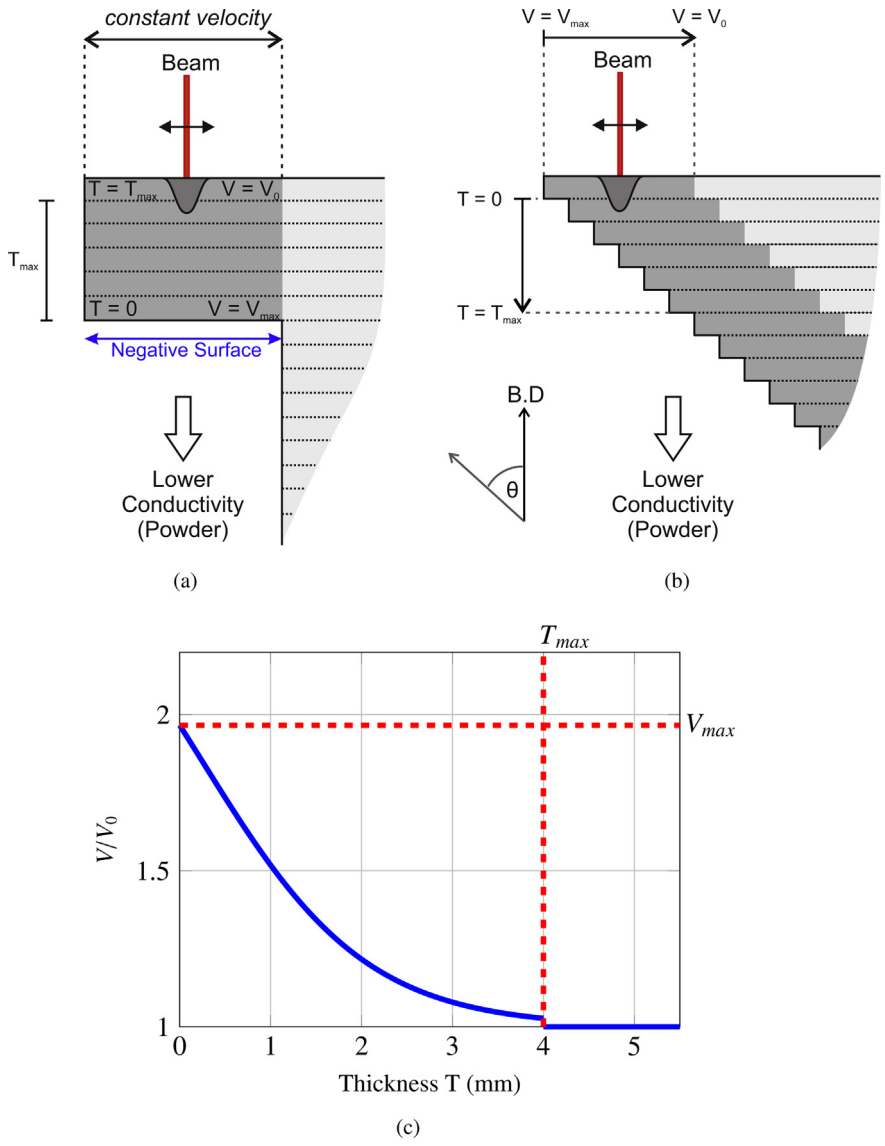

Fig. 2. Schematic diagram of the EBM process melting overhanging features for (a) a ledge type overhang and (b) truss element at an angle θ to the build direction (B.D). Darker regions show where the thickness function is active. (c) Shows the relative velocity profile with the default thickness function parameters.

the other three will not be discussed any further here. The reader is instead referred to Tammas-Williams et al. (2015) for further discussion on these functions.

The thickness function reduces the beam energy input by increasing the beam velocity rather than reducing the power, as the latter would require beam current changes at a rate that the system is not capable of attaining. The beam velocity V is altered as per the inverse exponential function of the thickness T in Eq. (1). T is defined as the vertical distance between the present layer and the negative surface beneath it. For a ledge overhang (Fig. 2a) the velocity will be maximum V_{max} at the negative surface ($T = 0$) and will then gradually reduce in the subsequent layers until the maximum preset thickness T_{max} is reached, upon which the velocity will return to its original value of V_0. For an angled specimen (Fig. 2b) the thickness will vary across each layer and thus so will the velocity. The distance L from the edge that the thickness function is active (darker region shown in Fig. 2b) for a specimen at an angle of θ to the build direction is easily calculated using Eq. (2).

$$\frac{V}{V_0} = 1 + \frac{S_f}{\exp(E_f(T - T_f)) + 1} \tag{1}$$

$$L = \frac{T_{\max}}{\tan(\theta)} \tag{2}$$

Three tuning parameters known as the Speed Factor (S_f), Exponent Factor (E_f) and Thickness factor (T_f) can be changed to adjust the profile, but for this study only the former two are of interest. The Speed Factor influences V_{max} and the Exponent factor influences the steepness of the profile between $T = 0$ and $T = T_{max}$. The Thickness factor and T_{max} will remain unchanged.

$$E = \frac{P}{Vht} \tag{3}$$

The resulting energy input changes from modifying the thickness function velocity profile would be quantified using the applied energy density parameter shown in Eq. (3). This has previously been used in the literature to benchmark changes made to key process attributes of powder bed systems i.e. beam power, beam velocity, line offset (spacing between hatch lines) and layer thickness (Thijs et al., 2010; Attar et al., 2014; Tammas-Williams et al., 2015). But as the changes to the thickness function will only result in changes to the beam velocity, this expression can be reduced to $E \propto V$. Comparisons between different parameter sets would be performed using

Table 1
The default and four modified parameter sets investigated.

Parameter set	Process parameters				$\left(\frac{E}{E_0}\right)_{avg}$
	S_f	E_f	T_f	T_{max} (mm)	
0 (default)	1.7	1.1	0.25	4	1.00
1	1.7	0			0.71
2	2.5	0			0.59
3	2.5	0.4			0.71
4	2.5	0.7			0.80

an average applied energy density across the region the thickness function is active (darker region in Fig. 2b), which would be calculated from the average velocity between $T = 0$ and $T = T_{max}$. This can be obtained by integrating Eq. (1) between these two limits and is shown in Eq. (4). The average energy densities for each modified thickness function parameter set can then be normalised against that of the default (E_{def}) in Eq. (5). For the default process parameters the average velocity ratio $(V/V_0)_{def}$ is 1.32

$$\left(\frac{V}{V_0}\right)_{avg} = 1 + S_f + \frac{S_f}{E_f T_{\max}} \log_e \left(\frac{\exp(-E_f T_f) + 1}{\exp(E_f T_{\max} - E_f T_f) + 1}\right) \quad (4)$$

$$\left(\frac{E}{E_{def}}\right)_{avg} = \frac{\left(V/V_0\right)_{avg}}{\left(V/V_0\right)_{def,avg}} \quad (5)$$

3. Experimental

3.1. Experimental builds

All three experimental builds detailed herein were performed using an Arcam A1 EBM machine using Ti–6Al–4V ELI powder and a layer thickness of 50 μm.

3.1.1. First build – benchmark experiment

To quantify the dimensional accuracy using default process parameters (listed in Table 1) a build comprising fifteen variations of the truss structure shown in Fig. 4a was first manufactured to provide a reference data set. Five angles to the build direction were investigated (θ = 20, 30, 40, 50 and 60°) each with three different truss diameters (D = 2, 5 and 10 mm), to observe the effects of both angle and diameter on dimensional accuracy which was quantified through measurement of mass. The lowest (θ = 20°) and highest (θ = 60°) angle specimens at 2 and 10 mm diameters were also assessed using laser scanning and X-ray Computed Tomography (XCT), allowing quantification of the member areas, second moment of areas and member curvature (detailed in Section 3.2).

3.1.2. Second build – process modification experiment

The second build contained groups of individual truss members with diameters of 2 and 10 mm at a constant angle to the build direction, which in this case was set to the maximum presented angle of 60°. An additional member with a square cross-section of side length 10 mm was also included in each group to assess the effect of geometry (if any). Groups of these three individual members would be manufactured for each of the thickness function parameter sets shown in Table 1 which include the default parameters ('0' - plotted in Fig. 2c) and four modified parameter sets that result in a lower average beam energy density. Parameter sets '1' and '2' investigate the use of a constant elevated velocity profile (Fig. 3a) whereas '3' and '4' investigate an inverse exponential velocity profile (Fig. 3b).

Because the thickness function is only applied in *hatching*, an additional five groups with the same parameters but without the use of *contouring* were also be fabricated. The prefix 'C' and 'NC' denotes specimens made with and without the use of *contouring* respectively. This build with all 10 groups is shown in Fig. 4b. The fabrication accuracy would be quantified through measurement of mass.

3.1.3. Third build – application of modified process parameters to benchmark truss structure

The modified parameters that resulted in the best dimensional accuracy were then applied to two of the benchmark truss structures (with θ = 60° and D = 2 and 10 mm). In addition a third set with the default parameters but with *contouring* disabled were also studied. Mass measurements and 3D scanning were performed so that any changes in dimensional accuracy resulting from these changes in process conditions could be compared with the results from the benchmark experiment.

3.2. Assessing dimensional accuracy from 3D scanning of fabricated specimens

To quantify the cross-sectional area, second moment of area and curvature along each member for selected specimens, laser scanning and XCT techniques were employed. A reasonably accurate 3-D surface representation could be created from each of these methods which could then aligned with that of the CAD model (a STereoLithography STL file). Once aligned, multiple planes perpendicular to the member centre lines of the CAD model were generated at equally spaced points along each member (shown schematically in Fig. 5b). The intersection of each of these planes with the scanned model would form closed polyline curves representing the member cross-sections (an example is shown in Fig. 5c).

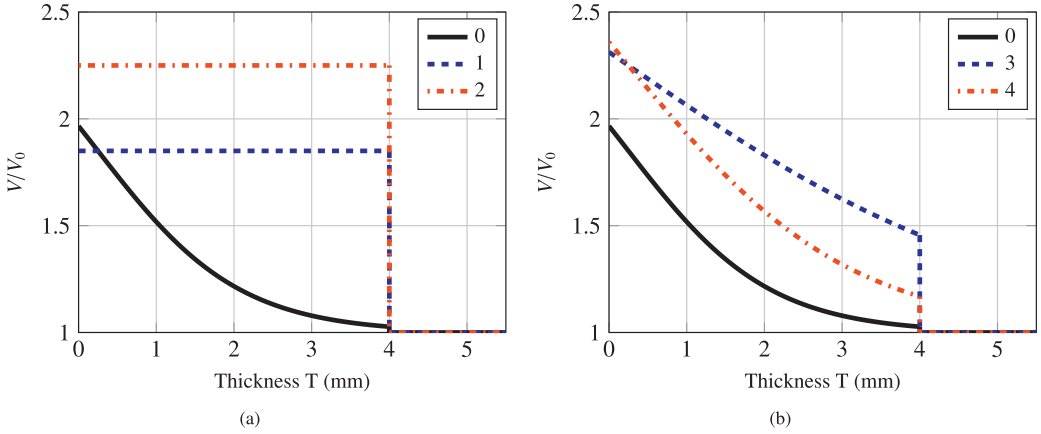

Fig. 3. Velocity ratio plots for (a) step functions '1' and '2' and (b) inverse exponential functions '3' and '4'. Default profile is denoted '0'.

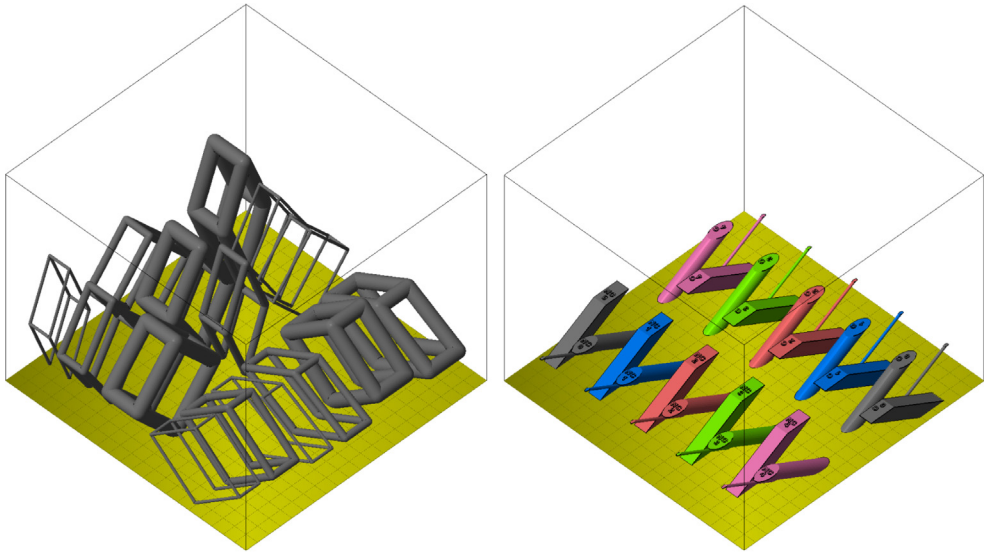

(a) (b)

Fig. 4. (a) Benchmark experiment and (b) process modification experiment.

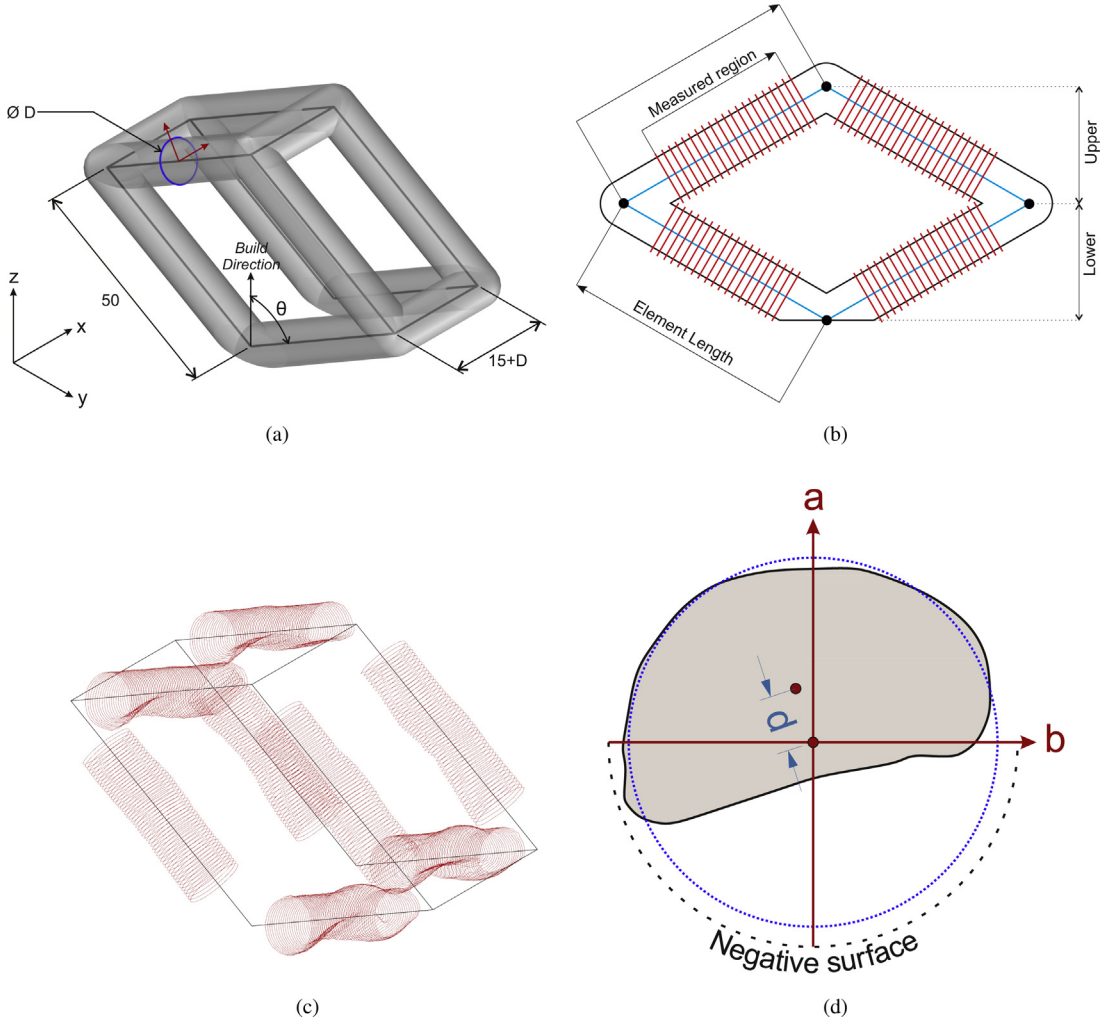

(a) (b)

(c) (d)

Fig. 5. (a) Dimensions of the benchmark truss structures, (b) schematic showing the location on the measuring planes which are normal to the member centre lines of the CAD model, (c) an example showing the polyline cross-sections obtained from these planes intersecting the scanned model and (d) the local coordinate system for each plane. The shaded region shows an example polyline cross-section and the dotted outline shows the cross-section of the CAD model.

Table 2
Area error (A_e), second moment of area error ($I_{b,e}$) and maximum curvature (δ_{max}) averaged for all 8 members of each of the benchmark truss structures. μ and σ denote the mean and standard deviation respectively.

Specimen		M_e (δ%)	A_e (δ%)		$I_{b,e}$ (δ%)		δ_{max} (mm)
θ (°)	D (mm)		μ	σ	μ	σ	
20	2	−10.2	−8.55	3.67	−14.2	5.76	0.176
	10	−4.60	3.64	1.81	−7.58	1.79	0.0739
60	2	−41.2	−40.2	11.3	−48.5	11.4	0.423
	10	−27.1	−25.5	11.3	−51.0	17.6	1.23

The coordinates of the polyline vertices were then used to calculate the area, second moment of area and the centroid of the cross-section. The latter would be used to calculate the linear distance between the centroid and the member centre line of the CAD model (labelled D in Fig. 5d), which would be the measure of effective curvature.

The coordinates of the vertices were first transformed from their global coordinates into the local plane coordinates 'a' and 'b' using Eqs. (6a) and (6b). This transformation ensures that the 'b' axis is aligned in such a way that it bisects the positive and negative surface of the member from the CAD model (illustrated in Fig. 5d). The area of each cross-section can then be calculated using Eq. (7). Following this the error in area and second moment of area about the 'b' axis can be calculated in Eqs. (8) and (9) respectively. The 'b' axis was chosen as the loss of material is on the negative surface hence the second moment of area about this axis should be the most affected. The curvature along the element δ, defined as the linear distance between the centroid of the scanned cross-section and the member centre line of the CAD model, is calculated in Eq. (10).

$$a_i = (v_i(x,y,z) - C_0(x,y,z)) \cdot (e_k \times \hat{x}) \tag{6a}$$

$$b_i = (v_i(x,y,z) - C_0(x,y,z)) \cdot (e_k \times \hat{z}) \tag{6b}$$

$$A = \frac{1}{2}\sum_{i=1}^{N}(a_i b_{i+1} - a_{i+1} b_i) \tag{7}$$

$$A_e = \frac{1}{A_0}(A - A_0) \tag{8}$$

$$I_{b,e} = \frac{1}{12 I_0}\left[\left(\sum_{i=1}^{N}\left(a_i - a_i a_{i+1} + a_{i+1}^2\right)(a_i b_{i+1} - a_{i+1} b_i)\right) - 12 I_0\right] \tag{9}$$

$$\delta = \frac{1}{6A}\left[\left(\sum_{i=1}^{N}(a_i + a_{i+1})(a_i b_{i+1} - a_{i+1} b_i)\right)^2 + \left(\sum_{i=1}^{N}(b_i + b_{i+1})(a_i b_{i+1} - a_{i+1} b_i)\right)^2\right]^{1/2} \tag{10}$$

C_0 are the coordinates of the intersection between the planes and the member centre lines of the CAD model, a_i and b_i are the local plane ordinates of each vertex i ($i = 1, \ldots, n$) which are calculated from the global coordinates v_i, e_k is the vector of the member centre line and $\hat{x}$ and $\hat{z}$ are unit x (1,0,0) and z (0,0,1) vectors, A is area of the resulting cross-section, A_0 and $I_{0,b}$ are the area and second moment of area (about local b axis) of the CAD model respectively, A_e and $I_{e,b}$ are the errors in area and second moment of area relative to that of the CAD model.

The 10 mm diameter specimens were scanned using a Metris LC15 laser scanner. The 2 mm diameter specimens were scanned using the Nikon Metris Custom Bay XCT apparatus at the University of Manchester Henry Mosely facility. All analyses used 100 intersecting planes per member.

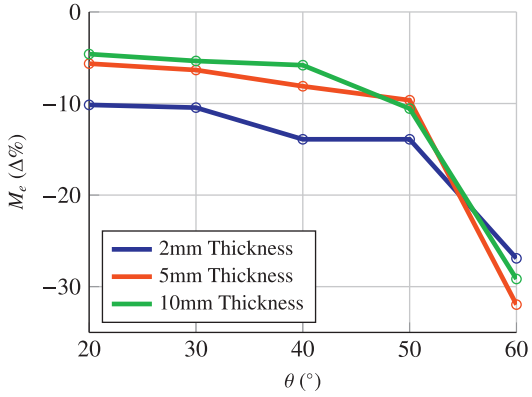

Fig. 6. Mass error (M_e) of fabricated specimens relative to their respective CAD models.

3.3. Metallurgical evaluation

To investigate the effect of process parameter adjustment on the internal structure of the experimental builds, selected specimens would be sectioned with a low speed precision cut-off wheel and prepared for metallurgical evaluation. Samples would initially be planar ground using water-lubricated SiC paper which would then be followed by the use of a 9 μm diamond suspension for the final grinding step. Final polishing of the specimens would be performed using colloidal silica suspension.

The size-distribution of internal features (either gas porosity of lack of fusion defects) was assessed optically by examining four regions of interest per condition to provide a total field of analysis of 16.8 mm^2 An automated thresholding procedure in the image analysis software ImageJ was employed to quantify the number and size (Feret Length) of defects.

4. Results

4.1. Benchmark experiment

The measured mass error (M_e) for all fifteen specimens are presented in Fig. 6 and the results of the 3D scanning analysis are given in Table 2. Here the mean average error and standard deviation of the area (A_e) and second moment of area ($I_{b,e}$) of all eight members for each structure has been calculated. The average of the maximum curvature (δ_{max}) of all 8 members per specimen is also shown.

Table 3
The resulting mass errors measured from each of the three geometries fabricated using the parameter sets shown in Table 1. The prefix 'C' denotes parameters sets that used *contouring* 'NC' denotes those that did not. An average mass error for all three geometries for each parameter set is also shown.

	Label	$\left(\frac{E}{E_0}\right)_{avg}$	M_e (δ%)			
			Circular		Square	Average
			10 mm	2 mm	10 mm	
Contouring enabled	C0	1.00	−35.9	−33.4	−30.5	−33.3
	C1	0.71	−28.6	−46.5	−23.7	−32.9
	C2	0.59	−16.7	−30.5	−14.9	−20.7
	C3	0.71	−24.7	−34.9	−18.7	−26.1
	C4	0.80	−28.2	−39.2	−23.0	−30.1
Contouring disabled	NC0	1.00	−14.3	−5.9	−12.3	−10.8
	NC1	0.71	−4.7	−8.8	−3.0	−5.5
	NC2	0.59	−4.9	−10.3	−3.7	−6.3
	NC3	0.71	−12.7	−11.7	−14.5	−13.0
	NC4	0.80	−19.2	−13.2	−16.5	−16.3

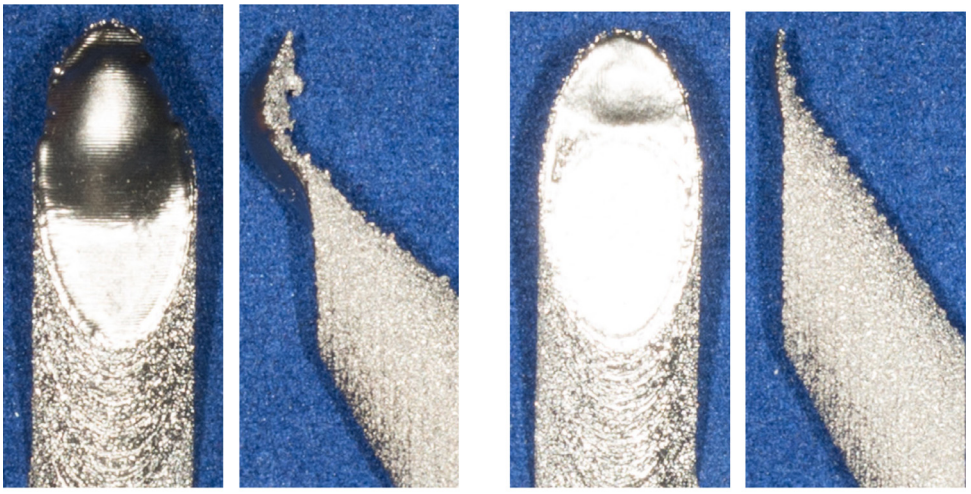

(a) (b)

Fig. 7. Photographs of two 10 mm diameter circular truss members fabricated with (a) the default parameter set – C0 and (b) C1 parameter set, viewed from the top (left) and side (right).

4.2. Process modification experiment

The mass error (M_e) for each of the three singular members in the ten sets are given in Table 3. Photographs taken of the 10 mm diameter circular members from the C0 and C1 sets are presented in Fig. 7.

4.3. Application of modified process parameters to benchmark truss structure

The two best parameter sets (as defined by those causing the lowest deviation in mass – NC1 and NC2) from Sec. 4.2 as well as the default parameters without *contouring* (NC0) were then used to manufacture the "benchmark" truss structure ($\theta = 60^\circ$ and diameter D = 2 and 10 mm). The resultant average mass error, area error, second moment of area error and maximum curvature for each specimen are given in Table 4. The variation of latter three parameters along the member lengths (grouped for the upper and lower members) is shown in Figs. 9 and 10 for the 2 and 10 mm diameter specimens respectively.

4.4. Porosity

The NC1 and NC2 cylindrical specimens (10 mm diameter) that were fabricated in the experiment detailed in Section 4.2, were

Table 4
The measured errors in mass (M_e), cross-sectional area (A_e), second moment of area error ($I_{b,e}$) and maximum curvature (δ_{max}) for the 2 and 10 mm diameter benchmark truss structures for each process parameter set. Note that M_e, A_e, $I_{b,e}$ and δ_{max} have been averaged over all 8 members for each specimen.

D (mm)	Parameter set	M_e (δ%)	A_e (δ%)		$I_{b,e}$ (δ%)		δ_{max} (mm)
			μ	σ	μ	σ	
2	C0	−41.2	−40.2	11.3	−48.5	11.4	0.423
	NC0	−9.0	−2.72	9.71	15.9	12.9	0.256
	NC1	−5.4	2.36	7.66	23.9	9.24	0.206
	NC2	−10.5	−0.39	4.23	18.6	14.3	0.281
10	C0	−27.1	−25.5	11.3	−51.0	17.6	1.23
	NC0	−17.2	−18.4	10.5	−41.5	18.0	0.613
	NC1	−5.5	6.35	3.26	6.18	9.51	0.139
	NC2	−2.8	9.12	1.40	13.8	4.10	0.108

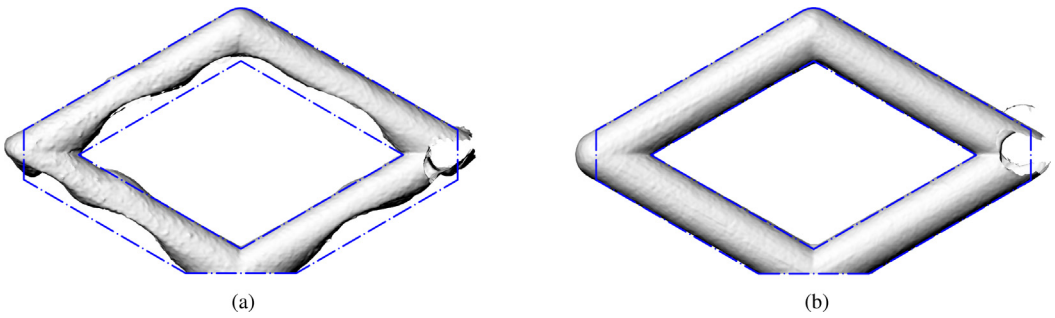

Fig. 8. Side profile of scan for the 10 mm diameter benchmark truss structure fabricate using (a) default C0 process parameters, (b) NC2 process parameters. Dashed outline shows the boundaries of the CAD model.

sectioned at the mid-point on a plane perpendicular to the member centreline and then prepared for optical microscopy as outlined in Section 3.3. The purpose of this analysis was to assess whether adjustments to the processing strategy to minimize mass loss also influenced the population of internal defects. Example micrographs illustrating the typical internal structure of specimen NC1 and NC2 are given Fig. 11. In both cases, large and irregular-shaped lack of fusion defects were observed along with sub-100 μm spherical

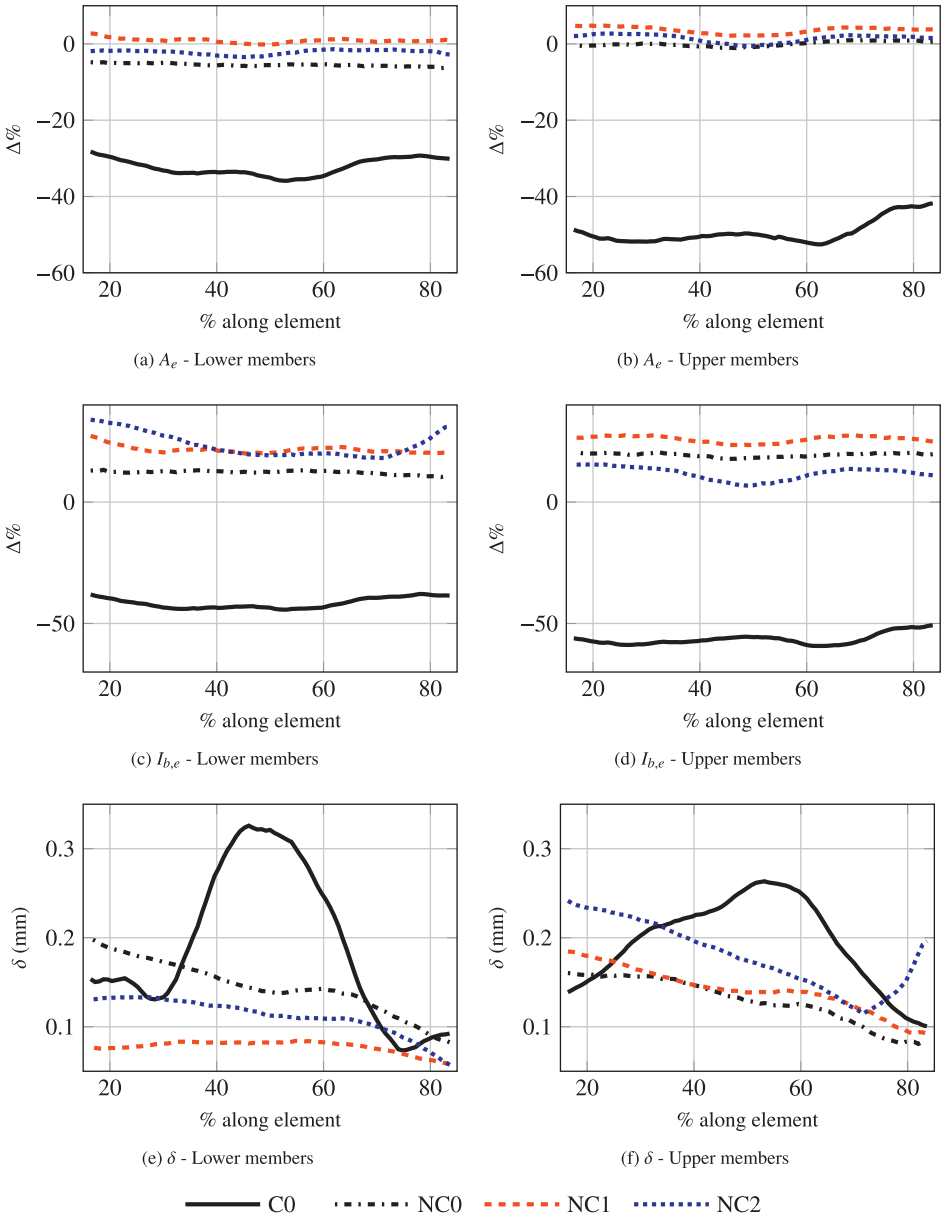

Fig. 9. The variation of the cross-sectional area error (A_e), second moment of area error ($I_{b,e}$) and curvature (δ) along the member lengths for the lower and upper members (denoted in Fig. 5d) of the 2 mm diameter benchmark truss structure. Shown in each plot is the average curve for the four members in each of these two groups.

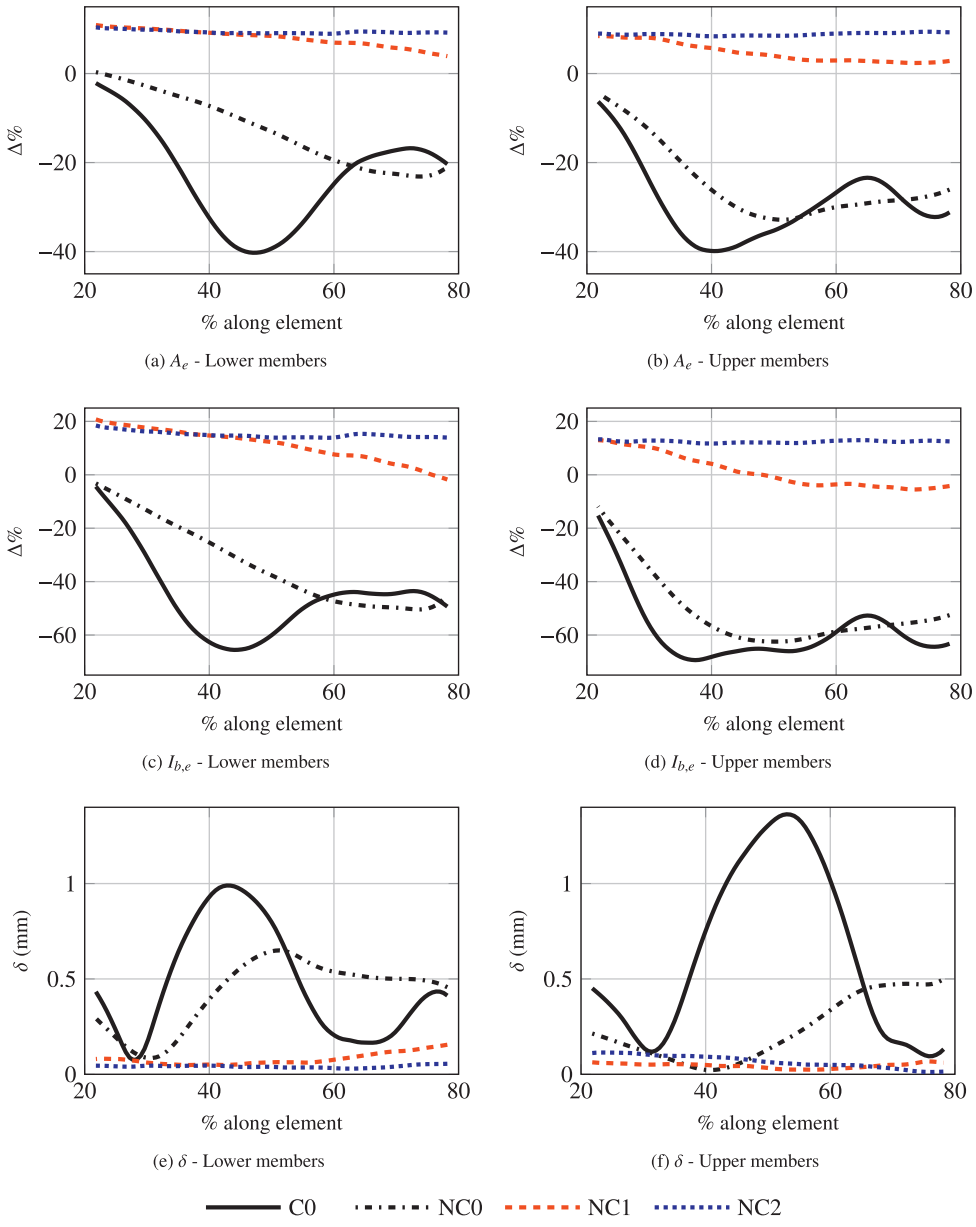

Fig. 10. The variation of the cross-sectional area error (A_e), second moment of area error ($I_{b,e}$) and curvature (δ) along the member lengths for the lower and upper members (denoted in Fig. 5d) of the 10 mm diameter benchmark truss structure. Shown in each plot is the average curve for the four members in each of these two groups.

pores, with the latter probably originating from the gas atomised feedstock powder.

Fig. 12 is an empirical cumulative probability plot showing the size distribution of internal defects sampled from specimens NC1 and NC2. Data was collected from equal areas of analysis from both specimens. Although the defects sampled from specimen NC1 are marginally larger (in terms of the distribution of Feret Lengths) than those sampled from NC2 on the whole, the number density of features observed per unit area of analysis (N_A) within NC1 is considerably smaller than in specimen NC2 (8.5 mm^{-2} versus 33.7 mm^{-2}).

5. Discussion

5.1. Overview

The EBM process will as a matter of course fabricate truss structures with dimensional errors if the beam energy input in close proximity to negative surfaces is not modified adequately, all fifteen truss structures in the benchmark experiment had undersized members. The magnitude of these errors increase with a greater relative orientation of the truss members to the build direction as shown in Fig. 6), however it has been demonstrated in this investigation that even for the worst observed case (60° to the build direction) the degree of inaccuracy can be mitigated significantly when the beam energy density is suitably reduced (−41.2% to −5.4% in one case with regard to the mass error).

The reason for the dimensional inaccuracy can be seen in the photographs of two specimens in Fig. 7. In Fig. 7a a single member has been fabricated using the default process parameters and this has resulted in a significant degree of distortion which has caused material to rise above what would have been the final layer during the build. The consequence of this "peeling up" effect is that powder will not have been properly deposited at this region in the subsequent layers. With the amount of heat input reduced, (Fig. 7b) it can be seen that the degree of part distortion is significantly lower

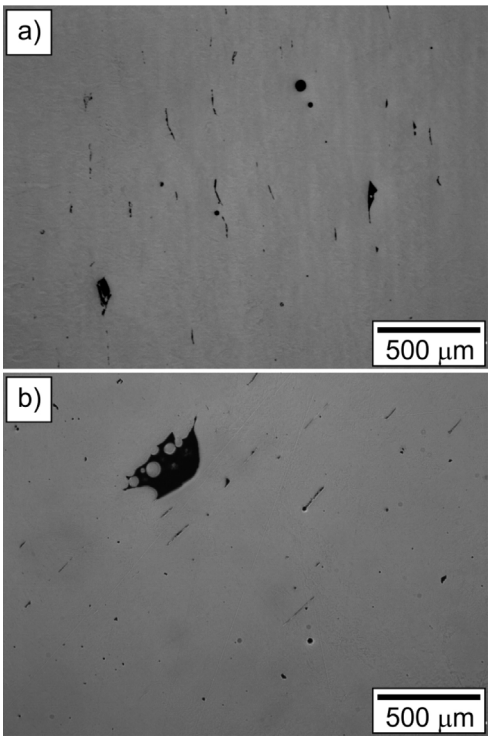

Fig. 11. Photographs obtained through optical microscopy for (a) the NC1 and (b) NC2 specimens.

and from the side there is visibly less material loss on the negative surface.

5.2. Benchmark experiment

The degree of the distortion becomes more prominent the greater the angle of the member orientation to the build direction, but as can be seen from Table 2 even members at a relatively small angle of 20° are still prone to this issue. In the case of the 2 mm diameter truss structure the average cross-sectional area and second moment of area errors were −8.6 and −14.2% which would result in an *equivalent* reduction in tensile/compressive strength and buckling capacity. At 60° however, these errors increase to −40.2 and −48.5% for the 2 mm specimens. The 10 mm specimens

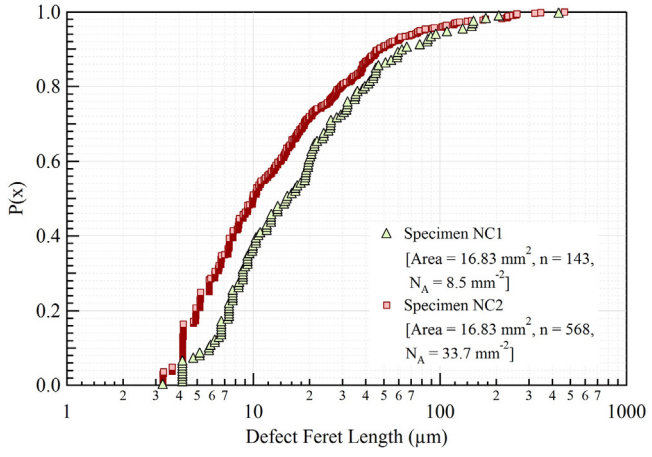

Fig. 12. Empirical cumulative probability plot showing the size distribution of defects sampled from specimens NC1 and NC2. The total area of analysis for each specimen is A = 16.83 mm^2, with n = total number of observed defects and N_A = calculated number density of defects per unit area of analysis.

at 20° are less compromised (A_e = −3.64 $I_{b,e}$ = −7.6%) whilst, in contrast to the 2 mm diameter trusses, at 60° this becomes even more significant (A_e = −25.5 $I_{b,e}$ = −51%) and a large effective curvature is introduced (δ_{max} = 1.23 mm).

What compounds these large errors in area, second moment of area and member curvature is that they are not consistent along the member lengths and would be hard to compensate for using scaling factors alone. This was especially true for the 10 mm diameter specimens where in Fig. 10 all three error measures (for C0) fluctuate significantly along the members lengths. This almost sinusoidal fluctuation can also be observed directly from the visual representation obtained from the 3D scan as shown in Fig. 8a.

5.3. Process modification experiment

The data in Table 3 reveals that a reduction in the average beam energy density resulted in a reduced mass error, but what is more striking is that samples fabricated without the use of *contouring* were significantly more accurate than those fabricated with both *contouring* and *hatching*. This is most obvious with the NC0 parameters where, still using the default thickness function velocity profile, the average mass error for the three geometries was reduced from −33.3% to −10.8%. Even more noticeable is that the 2 mm diameter specimen was fabricated most accurately when using the default thickness function profile without *contouring*. Although this is perhaps not too surprising as the contour stage in these specimens is melting a far larger proportion of the area, and the thickness function does not apply to this stage of the melting process. With no compensation for the lower conductivity of the powder beneath negative surfaces, the contour stage is depositing an excess energy into these regions.

Of the two types of velocity profile explored, those with a constant velocity yielded the better results than those employing the velocity scaling function given in Eq. (1). In fact the NC1 and NC3 specimens had the same average energy density but the former using a constant velocity profile proved the more accurate of the two. This highlights the importance of the beam velocity profile as well as the overall quantity of energy input.

5.4. Application of modified process parameters to benchmark truss structure

Both the constant velocity profiles NC1 and NC2 were applied to the fabrication of two variations of the benchmark truss structures (θ = 60° for D = 2 and 10 mm) with very promising results. First of all it can be seen in Table 4 that the average for all three error measures has been dramatically reduced over the default C0 parameters. For the 10 mm specimens a reduction from −25.5% to +6.35% was found when using the NC1 parameters. As with the experiment discussed in Section 5.3 most of the improvement with the 2 mm diameter specimens were achieved through disabling *contouring*, with marginal differences between the NC0, NC1 and NC2 parameters.

Whilst NC1 resulted in slightly lower average errors for the 10 mm diameter specimens, it can be seen in Fig. 10 that these error measures were more consistent along the member lengths for NC2. What is also noticeable is that both the NC1 and NC2 produce oversized members. As the second moment of area is proportional to the cross-sectional area squared, this error is particularly large (13.8% for NC2), but this is most probably caused by the lack of a proper offset in place between the *hatching* path and the boundary of the cross-section of the part i.e. the beam is melting material outside of the perimeter defined by the CAD model. Because the error is consistent along the member lengths a simple remedy for this would be the implementation of such an offset, this being a trivial matter to achieve.

The effective curvature of the 2 mm diameter members was difficult to determine in an absolute manner as the specimens may have been deformed when being manipulated for scanning. This could potentially be the reason for the great variation in Figs. 9e and f, nevertheless the effective curvature has been approximately halved for all three non-contour parameter sets NC0, NC1 and NC2 as compared with their *contoured* equivalents C0, C1 and C2. For the sturdier 10 mm samples, when compared to the default C0 parameters the curvature has been reduced by 89 and 91% for NC1 and NC2 respectively, and as can be seen in Fig. 10e and f the curvature along the length of the members is very low.

The improvements in dimensional accuracy are most easily observed in Fig. 8 where the side profiles of the laser scanned C0 and NC2 specimens are shown with an overlay of the CAD model.

5.5. Porosity

Although the NC1 specimen had a decreased defect population density versus NC2 the size of the features are still unacceptably large. For both of these parameter sets there is clearly insufficient heat input per unit volume of material on the powder bed to guarantee a fully dense part. Further modifications to these parameters would therefore aim to determine the energy density that yields an effective compromise between high dimensional accuracy and a low defect population density. Referring back to Eq. (3) this would involve further modification to the beam velocity and/or changes to the line offset (distance between hatch lines). Changes to the T_{max} variable should also be investigated as this determines the proportion of the melt area for which the thickness function is active (as per Eq. (2)) and this was also where the large lack of fusion defects commonly appeared. It should be noted that the defect population data acquired from both specimens was sampled from two-dimensional planar cross-sections. The use of Micro XCT analysis, which could consider the whole volume, would considerably increase the reliability of the data.

The pores seen with the NC1 and NC2 parameters could be easily eliminated (or at least significantly reduced) by Hot Isostatic Pressing. Even parts with the more commonly observed sub 100 μm pores would require this step to ensure acceptable fatigue life, but it must be accepted that HIP routines do result in a slight reduction in tensile strength due to coarsening of the Widmanstatten alpha lath structure (Al-Bermani et al., 2010).

Furthermore, as there is considerable variance in the microstructure and mechanical properties of material produced via EBM technologies, standards are required against which the microstructure and mechanical performance of EBM components can be benchmarked (Thomas and Baxter, 2015), particularly in parts subjected to cyclic loads where the occurrence of microstructural aberrations severely influence fatigue life. This work therefore clearly highlights the need for careful control of the key process variables in order to obtain both a dimensionally accurate and microstructurally sound component, irrespective of whether the structure is optimised for weight or not.

6. Conclusions

- All truss members at an angle to the build direction fabricated with the default process parameters provided by the manufacturer Arcam were undersized. This issue is exacerbated as the angle to the build direction increases.
- Compensating for these errors using linear scaling factors would be ineffective as magnitude of the errors vary considerably along the truss members.
- The reason for this inaccuracy was observed to be an excessive beam energy density at regions in proximity to negative surfaces. This resulted in part distortion that compromised the powder deposition and melting stages in the subsequent layers.
- Reducing the beam energy density by increasing the beam velocity of the hatch melt stage when melting in proximity to a negative surface and discarding the contour stage during melting resulted in significant improvements in dimensional accuracy.
- But in reducing the energy density there was an increase in the number and size of pores present due to lack of fusion in localised regions.
- These pores could be eliminated using HIP routines, a step that would also be required to eliminate the sub 100 μm spherical pores more commonly observed in EBM parts.
- Further refinement of the process modifications detailed herein would seek to find the energy input that is an acceptable balance between good dimensional accuracy and low defect population density.

Acknowledgements

The first author acknowledges the sponsorship of the Advanced Metallic Systems Centre for Doctoral Training, an EPSRC funded centre involving the Universities of Sheffield and Manchester. The first author also acknowledges the Henry Moseley facility at the University of Manchester.

References

Al-Bermani, S.S., Blackmore, M.L., Zhang, W., Todd, I., 2010 Aug. The origin of microstructural diversity, texture, and mechanical properties in electron beam melted Ti–6Al–4V. Metall. Mater. Trans. A 41 (13), 3422–3434, http://dx.doi.org/10.1007/s11661-010-0397-x.

Attar, H., Calin, M., Zhang, L., Scudino, S., Eckert, J., 2014. Manufacture by selective laser melting and mechanical behavior of commercially pure titanium. Mater. Sci. Eng. A 593, 170–177 http://www.sciencedirect.com/science/article/pii/S0921509313012665.

Bauereiß, A., Scharowsky, T., Körner, C., 2014 Nov. Defect generation and propagation mechanism during additive manufacturing by selective beam melting. J. Mater. Process. Technol. 214 (11), 2522–2528. http://linkinghub.elsevier.com/retrieve/pii/S0924013614001691.

Cansizoglu, O., Harrysson, O.L., West II, H.A., Cormier, D.R., Mahale, T., 2008. Applications of structural optimization in direct metal fabrication. Rapid Prototyp. J. 14 (2), 114–122, http://dx.doi.org/10.1108/13552540810862082.

Cooke, A.L., Soons, J.A., 2010. Variability in the geometric accuracy of additively manufactured test parts national institute of standards and technology, Gaithersburg, MD, USA. In: SFF symposium, Austin, pp. 1–12.

Edwards, P., O'Conner, a., Ramulu, M., 2013 Nov. Electron beam additive manufacturing of titanium components: properties and performance. J. Manuf. Sci. Eng. 135 (6), 061016, http://dx.doi.org/10.1115/1.4025773.

Rozvany, G.I.N., 2009. A critical review of established methods of structural topology optimization. Struct. Multidiscipl. Optim., 217–237.

Schevenels, M., Lazarov, B., Sigmund, O., 2011. Robust topology optimization accounting for spatially varying manufacturing errors. Comput. Methods Appl. Mech. Eng. 200 (December (49–52)), 3613–3627 http://linkinghub.elsevier.com/retrieve/pii/S0045782511002611.

Sigmund, O., Maute, K., 2013, August. Topology optimization approaches. Struct. Multidiscipl. Optim., 1031–1055, http://dx.doi.org/10.1007/s00158-013-0978-6.

Smith, C.J., Gilbert, M., Todd, I., Derguti, F., 2015. Application of layout optimization to the design of additively manufactured metallic components. Struct. Multidiscipl. Optim. (in press).

Tammas-Williams, S., Zhao, H., Léonard, F., Derguti, F., Todd, I., Prangnell, P., 2015. XCT analysis of the influence of melt strategies on defect population in Ti–6Al–4V components manufactured by selective electron beam melting. Mater. Charact. 102, 47–61 http://linkinghub.elsevier.com/retrieve/pii/S104458031500039X.

Thijs, L., Verhaeghe, F., Craeghs, T., Humbeeck, J.V., Kruth, J.-P., 2010 May. A study of the microstructural evolution during selective laser melting of Ti–6Al–4V. Acta Mater. 58 (9), 3303–3312 http://linkinghub.elsevier.com/retrieve/pii/S135964541000090X.

Thomas, M., Baxter, G., 2015. Recommendations for Validation & Mechanical Testing of Additive Manufactured Components. Rolls-Royce Technical Report RET101687.